Extracting the pairing gap from van Hove singularities in rf spectra of the Fermi-Hubbard model

Chuping Li,[1,2,3] Kaichao Zhang,[1,2,3] Junru Wu,[1,2,3] Yuxuan Wu,[1,2,3] Dingli Yuan,[1,2,3] Pengyi Chen,[1,2,3] Lin Sun,[3,2,*] and Qijin Chen[1,2,3,†]

[1]*Hefei National Research Center for Physical Sciences at the Microscale and School of Physical Sciences, University of Science and Technology of China, Hefei, Anhui 230026, China*

[2]*Shanghai Research Center for Quantum Science and CAS Center for Excellence in Quantum Information and Quantum Physics, University of Science and Technology of China, Shanghai 201315, China*

[3]*Hefei National Laboratory, University of Science and Technology of China, Hefei 230088, China*

(Received 7 August 2026; accepted 14 October 2026; published 12 November 2026)

We show that van Hove singularities in radio-frequency spectra of the three-dimensional (3D) attractive Fermi-Hubbard model provide a robust route to extracting the pairing gap. Four types of singularities are classified, and their spectral positions are shown to depend solely on the pairing gap Δ and chemical potential μ through simple algebraic relations. Measuring two well-resolved singularities therefore determines both parameters without requiring full spectral fitting. Numerical simulations incorporating phenomenological lifetime and scattering broadenings confirm that these features remain visible in both momentum-integrated and k_z-integrated spectra, and become more pronounced at stronger coupling where conventional backbending methods lose sensitivity. At half filling, particle-hole symmetry fixes μ, reducing the extraction to a single singularity measurement. These results establish van Hove singularity analysis as a practical spectroscopic diagnostic for pairing in quantum-simulated 3D Fermi-Hubbard systems.

DOI: 10.1103/mthq-q8kh

I. INTRODUCTION

Ultracold Fermi gases in optical lattices have garnered significant attention over the past two decades, as their high degree of tunability renders them an ideal platform for quantum simulation and engineering. These systems offer substantial potential for advancing our understanding of long-standing problems in condensed matter physics and exploring novel regimes of quantum matter [1–6]. The versatility of these platforms arises from the precise control over parameters such as interaction strength, lattice depth, temperature, dimensionality, population imbalance, and lattice geometry. In particular, the transition from Bardeen-Cooper-Schrieffer (BCS) superfluidity to Bose-Einstein condensation (BEC) of fermion pairs, namely, the BCS-BEC crossover, can be realized by tuning the effective interaction strength through a Feshbach resonance in trapped atomic Fermi gases [7,8]. This crossover is intimately linked to the pseudogap phenomenon observed in cuprate superconductors [9], a topic of paramount importance for elucidating the mechanisms of high-temperature superconductivity [10,11].

The physics of ultracold Fermi gases in a three-dimensional optical lattice (3DOL) can be described by the Fermi-Hubbard model (FHM). However, despite extensive theoretical effort [12–19], the phase diagram of the three-dimensional (3D) attractive FHM at intermediate and strong coupling, especially at high fillings, remains largely undetermined. In the weak-coupling limit, BCS mean-field theory, along with the Gor'kov correction [20], provides a reliable description. In the BEC regime at low densities, the physics reduces to a dilute gas of tightly bound pairs whose few-body properties are well understood. Away from these limiting regimes, however, in the intermediate coupling and density range where pairing fluctuations are the most prominent, diagrammatic methods capture qualitative trends but differ quantitatively in their predictions for key observables such as the pairing gap Δ. For instance, the non-self-consistent G_0G_0 approximation [21], widely used for its computational simplicity, the G_0G scheme (derived using an equation-of-motion approach [22,23], employed in the present work), and the conserving GG theory [24–26] each yield appreciably different values of Δ in the pseudogap regime where the effects of pairing fluctuations are strong. Often regarded as a reliable numerical method, quantum Monte Carlo, which is free of the fermion sign problem in the attractive case, is limited by the analytic continuation needed to obtain real-frequency spectral information, which obscures fine spectral features at strong coupling. In addition, it suffers from numerical instability at strong coupling and becomes computationally prohibitive at large lattice sizes and low temperatures. Consequently, quantum simulation experiments that realize the 3D attractive FHM in controllable cold-atom platforms [27–31] are

*Contact author: lsun22@ustc.edu.cn
†Contact author: qjc@ustc.edu.cn

Published by the American Physical Society under the terms of the Creative Commons Attribution 4.0 International license. Further distribution of this work must maintain attribution to the author(s) and the published article's title, journal citation, and DOI.

indispensable for establishing the phase diagram, and recent progress, including measurements of the doublon fraction [32], underscores the need for complementary diagnostics that can directly extract pairing parameters from spectroscopic measurements. This work develops such a diagnostic.

In particular, radio-frequency (rf) spectroscopy serves as an important probe for investigating superfluid pairing physics and has been widely used in experiments on ultracold Fermi gases [33,34]. Initially utilized to probe mean-field shifts in strongly interacting systems, the technique evolved following the proposal that the pairing gap could be extracted spectroscopically [35]. Subsequent experiments have provided compelling evidence of fermionic pairing through distinct spectral signatures [36–38]. Nevertheless, the peak position in momentum-integrated rf spectra can hardly be used to extract the pairing gap, since the fermion energy shift induced by pairing is momentum dependent and not proportional to the gap [39].

Momentum-resolved rf spectroscopy, analogous to angle-resolved photoemission spectroscopy, overcomes this limitation by directly measuring the spectral function $A(\mathbf{k}, \omega)$ [40–42]. In homogeneous continuum gases, the pairing gap can then be inferred from the characteristic backbending of the dispersion, a technique that has recently confirmed the presence of a pseudogap in strongly interacting Fermi gases [43].

In optical lattices, however, the anisotropic dispersion makes the direct reconstruction of full 3D momentum-resolved rf spectra experimentally demanding. Such measurements have been successfully demonstrated in two-dimensional lattice systems [31], but extending them to three dimensions remains beyond reach at present. Theoretical studies of rf spectroscopy in the attractive Hubbard model have also been limited [44]. Consequently, it is desirable to identify spectral markers that survive partial momentum integration and whose positions are directly linked to the underlying pairing parameters.

In this work, we investigate the effects of van Hove singularities (vHSs) in both momentum-integrated and momentum-resolved rf spectra for two-component ultracold Fermi gases in a 3DOL with nearest-neighbor hopping, described by an attractive Fermi-Hubbard model. The vHS features originate from the underlying lattice band structure and are subsequently modified by fermion pairing. We show that, within the present approximation, the spectral positions of the vHS features are controlled by the pairing gap Δ and the effective chemical potential μ, defined precisely in Sec. II. In principle, measuring two well-resolved vHS positions therefore allows one to infer both Δ and μ from the corresponding algebraic relations. This strategy is complementary to conventional analyses based on rf spectral peaks and the backbending of the quasiparticle dispersion: Because the vHS positions are fixed by lattice critical points, they remain robust and identifiable even when the momentum is only partially resolved in the rf spectra. Employing the G_0G T-matrix approximation within the framework of pair-fluctuation theory [45], we solve the 3D attractive FHM at finite temperature T and fermion density n for different interaction strengths U. We introduce two phenomenological broadening parameters into the self-energy to simulate momentum-integrated and momentum-resolved rf spectra under realistic experimental conditions [46,47]. Because momentum-resolved rf measurements typically involve integration over one momentum component (line-of-sight integration), we also calculate the k_z-integrated momentum-resolved spectrum and identify the four types of vHSs in these rf spectra, each appearing at distinct rf detunings. For illustrative purposes, we keep the main text focused on the representative cases $n = 0.1$ and $n = 1$. Additional results for intermediate fillings ($n = 0.2, 0.4, 0.6, 0.8$) and interaction strengths are shown in Appendix B. The detailed self-consistent equations are also provided in Appendix A.

II. THEORETICAL FORMALISM

A. Model and overview of the pairing fluctuation theory

The attractive FHM in momentum space is described by

$$H-\mu\hat{N} = \sum_{\mathbf{k}\sigma} \xi_{\mathbf{k}} \hat{c}^{\dagger}_{\mathbf{k}\sigma} \hat{c}_{\mathbf{k}\sigma} + U \sum_{\mathbf{k}\mathbf{k}'\mathbf{q}} \hat{c}^{\dagger}_{\mathbf{k}_+\uparrow} \hat{c}^{\dagger}_{-\mathbf{k}_-\downarrow} \hat{c}_{-\mathbf{k}'_-\downarrow} \hat{c}_{\mathbf{k}'_+\uparrow},$$

where $\xi_{\mathbf{k}} = \epsilon_{\mathbf{k}} - \mu$, $\mathbf{k}_{\pm} \equiv \mathbf{k} \pm \mathbf{q}/2$, and μ is the effective fermion chemical potential into which the mean-field Hartree shift has already been absorbed. Here, $U < 0$ is the attractive interaction strength, and $\epsilon_{\mathbf{k}} = 2t(3 - \cos k_x - \cos k_y - \cos k_z)$ is the tight-binding dispersion, where t is the nearest-neighbor hopping amplitude and the lattice constant is set to unity. Throughout this work, we take the half bandwidth $6t$ as the energy unit.

We solve the attractive FHM using the G_0G scheme of the T-matrix approximation of pair-fluctuation theory, which self-consistently includes pairing fluctuations beyond mean-field BCS theory, as derived from the earlier work of Kadanoff and Martin [22]. The full formalism is detailed in Refs. [39,45] and in Appendix A; here, we only outline the essential physical structure.

The fermion self-energy $\Sigma(K) = \Sigma_{\rm sc}(K) + \Sigma_{\rm pg}(K)$ contains in general contributions from both zero-momentum pairing (relevant below T_c, giving rise to the superfluid condensate contribution $\Sigma_{\rm sc}$) and finite-momentum pairing. The latter, referred to as the pseudogap self-energy, is expressed through the T-matrix $t_{\rm pg}(Q) = U/[1 + U\chi(Q)]$, where $\chi(Q) = \sum_K G_0(Q-K)G(K)$ is the pair susceptibility. Near T_c, the dominant contribution to $\Sigma_{\rm pg}$ comes from the vicinity of $Q = 0$, allowing the pseudogap to be captured by a single energy scale $\Delta^2_{\rm pg} = -\sum_{Q\neq 0} t_{\rm pg}(Q)$. The total pairing gap $\Delta = \sqrt{\Delta^2_{\rm sc} + \Delta^2_{\rm pg}}$ enters a BCS-like gap equation and particle-number equation [Eqs. (A6) and (A7)], which are solved self-consistently for μ, $\Delta_{\rm sc}$, and $\Delta_{\rm pg}$ at given U, n, and T. The resulting Green's function takes the standard BCS form

$$G(K) = \frac{u_k^2}{i\omega_l - E_{\mathbf{k}}} + \frac{v_k^2}{i\omega_l + E_{\mathbf{k}}}, \tag{1}$$

with coherence factors $u_k^2, v_k^2 = (1 \pm \xi_{\mathbf{k}}/E_{\mathbf{k}})/2$ and $E_{\mathbf{k}} = \sqrt{\xi_{\mathbf{k}}^2 + \Delta^2}$.

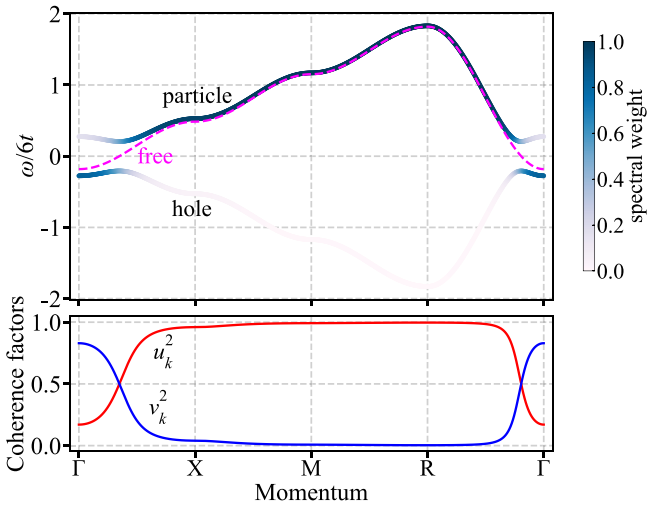


FIG. 1. Representative spectral function of the 3D attractive FHM at U_c and T_c for $n = 0.1$. The results are obtained from self-consistent solutions yielding $\Delta = 0.207$ and $\mu = 0.182$ (in units of $6t$). The upper and lower blue curves denote the particle and hole quasiparticle branches, respectively, with the two branches color coded by their spectral weight. The dispersions are plotted along the high-symmetry lines of the first Brillouin zone, with $\Gamma = (0, 0, 0)$, $\mathrm{X} = (\pi, 0, 0)$, $\mathrm{M} = (\pi, \pi, 0)$, and $\mathrm{R} = (\pi, \pi, \pi)$. The magenta curve represents the noninteracting band dispersion. The lower panel shows the coherence factors $u^2_{\mathbf{k}}$ and $v^2_{\mathbf{k}}$, corresponding to the spectral weights of the two quasiparticle branches.

B. Spectral function and van Hove singularities

The spectral function $A(\mathbf{k}, \omega)$ follows directly from Eq. (1) as

$$A(\mathbf{k}, \omega) = -2\,\mathrm{Im}\, G^{\mathrm{R}}(\mathbf{k}, \omega) = 2\pi\left[u^2_{\mathbf{k}}\delta(\omega - E_{\mathbf{k}}) + v^2_{\mathbf{k}}\delta(\omega + E_{\mathbf{k}})\right], \tag{2}$$

exhibiting two quasiparticle branches with weights given by the coherence factors.

Figure 1 illustrates a typical spectral function for a Fermi gas at critical coupling $U_c \approx -7.9136t$ in a 3DOL, corresponding to the threshold for forming a two-body bound state with zero binding energy in the dilute limit. The upper and lower branches correspond to the "particle" and "hole" quasiparticles, respectively. As depicted in the lower panel, the coherence factors $u^2_{\mathbf{k}}$ and $v^2_{\mathbf{k}}$ dictate the spectral weights of these quasiparticles at energies $\pm E_{\mathbf{k}}$. The locus $\xi_{\mathbf{k}} = 0$ for free fermions defines the Fermi surface. A comparison between the quasiparticle dispersion and the noninteracting band dispersion reveals a distinct pairing gap opening at the Fermi surface, whose crossing with the quasiparticle dispersion is located midway along the Γ–X and Γ–R paths.

A van Hove singularity, associated with a nonanalytic feature in the density of states (DOS) $N(\omega) = \sum_{\mathbf{k}} A(\mathbf{k}, \omega)$ [48], arises from the vanishing gradient of the lattice dispersion, $\nabla_{\mathbf{k}}\xi_{\mathbf{k}} = 0$. For a standard 3D cubic lattice, the Hessian matrix $\mathcal{H}(\xi_{\mathbf{k}})$ evaluated at the critical points is diagonal:

$$\mathcal{H}(\xi_{\mathbf{k}}) \propto \begin{bmatrix} \cos k_x & 0 & 0 \\ 0 & \cos k_y & 0 \\ 0 & 0 & \cos k_z \end{bmatrix}.$$

When $k_{x,y,z}$ take values 0 or π, four distinct types of vHSs arise, including a local minimum (M_0, all cosines positive), a local maximum (M_3, all cosines negative), and two types of saddle points (M_1 and M_2, with mixed signs). Along the dispersion shown in Fig. 1, the Γ, X, M, and R points correspond to these four vHS types, respectively, i.e., $(\Gamma, \mathrm{X}, \mathrm{M}, \mathrm{R}) \leftrightarrow (\mathrm{M}_0, \mathrm{M}_1, \mathrm{M}_2, \mathrm{M}_3)$.

C. rf response and vHS kinematic relations

Within linear response theory, the lowest-order rf current for a transition from an initial interacting state to a final noninteracting state is [39]

$$I(\nu) = \frac{1}{2\pi}\sum_{\mathbf{k}} A(\mathbf{k}, \omega) f(\omega)|_{\omega = \xi_{\mathbf{k}} - \nu}, \tag{3}$$

where ν is the rf detuning and $f(\omega) = 1/(e^{\omega/T} + 1)$ is the Fermi-Dirac distribution function, with $k_B = 1$. The energy-conservation constraint $\omega = \xi_{\mathbf{k}} - \nu$ reveals a structural resemblance between the rf response and the DOS, suggesting that vHS signatures will also manifest in the rf spectroscopy of lattice Fermi gases.

At low temperatures, the particle branch is exponentially suppressed by the Fermi function. Focusing on the hole branch and substituting into Eq. (3) gives

$$I_h(\nu) = \int \frac{\mathrm{d}^3 k}{(2\pi)^3} v^2_{\mathbf{k}} f(\xi_{\mathbf{k}} - \nu)\delta(\xi_{\mathbf{k}} - \nu + E_{\mathbf{k}}). \tag{4}$$

By imposing the resonance condition $\xi_{\mathbf{k}} - \nu + E_{\mathbf{k}} = 0$ at the four vHS momenta, the characteristic rf detunings of the vHS are obtained as

$$\mathrm{M}_0 : \nu_0 = -\mu + \sqrt{\mu^2 + \Delta^2}, \tag{5a}$$

$$\mathrm{M}_1 : \nu_1 = \frac{2}{3} - \mu + \sqrt{\left(\frac{2}{3} - \mu\right)^2 + \Delta^2}, \tag{5b}$$

$$\mathrm{M}_2 : \nu_2 = \frac{4}{3} - \mu + \sqrt{\left(\frac{4}{3} - \mu\right)^2 + \Delta^2}, \tag{5c}$$

$$\mathrm{M}_3 : \nu_3 = 2 - \mu + \sqrt{(2 - \mu)^2 + \Delta^2}, \tag{5d}$$

in units of $6t$. The band energies at the vHS points are $\epsilon_i = 2i/3$ $(i = 0, 1, 2, 3)$, i.e., $\epsilon_0 = 0$, $\epsilon_1 = 2/3$, $\epsilon_2 = 4/3$, and $\epsilon_3 = 2$. Equivalently, the four detunings can be combined into the unified expression

$$\nu_i = \epsilon_i - \mu + \sqrt{(\epsilon_i - \mu)^2 + \Delta^2}, \quad i = 0, 1, 2, 3. \tag{6}$$

Equation (5) are the central result of this analysis: The rf detuning of each vHS is determined by μ and Δ within the BCS-like quasiparticle description, with additional self-energy shifts either negligible or absorbed into these parameters. Since there are only two unknowns, measuring any two well-resolved vHS positions suffices to determine both parameters algebraically. In the special case of half filling ($n = 1$), particle-hole symmetry pins $\mu = 1$, so that a single measured vHS uniquely determines Δ.

The inversion in Eq. (5) is valid whenever the quasiparticle propagator retains a BCS-like pole structure, with a real, momentum-independent gap Δ and all diagonal self-energy

corrections absorbed into an effective μ. Within the present pair-fluctuation theory, this holds when the pair susceptibility is dominated by the long-wavelength ($Q \approx 0$) mode, i.e., below and in the vicinity of T_c, so that the pseudogap self-energy reduces to a single self-consistently determined scalar Δ_{pg}. Because the relation is purely kinematic, following from the resonance condition at a lattice critical point, it holds in this form for any many-body scheme whose propagator retains such a pole structure, although the numerical values of Δ and μ it returns are specific to the scheme used to obtain them. It would thus apply, e.g., to the G_0G_0 [21,49] and GG [24,50] formulations of the T-matrix approximation for pairing, provided they arrive at a BCS-like dispersion. For other forms of the self-energy treatment, one may arrive at different relations between the vHS positions and (Δ, μ); the extraction strategy itself, however, remains valid.

Experimentally, one can achieve momentum resolution in the xy plane by shining the imaging laser in the k_z direction. This leads to a k_z-integrated spectral response, given by integrating Eq. (4) over k_z:

$$I_h(k_x, k_y, \nu) = \frac{1}{\pi^3}\int_0^\pi \mathrm{d}k_z\, v_{\mathbf{k}}^2 f(\xi_{\mathbf{k}} - \nu)\delta(\xi_{\mathbf{k}} - \nu + E_{\mathbf{k}}) = \frac{1}{(2\pi)^3}\frac{\Delta^2}{\nu^2}\left[1 - f\left(\frac{\nu^2 + \Delta^2}{2\nu}\right)\right]\frac{3}{|\sin k_{z_0}|}, \quad (7)$$

where $k_{z_0}(k_x, k_y, \nu)$, defined as the root of $\xi_{\mathbf{k}} - \nu + E_{\mathbf{k}} = 0$ for given k_x, k_y, and ν, signals a vHS when $k_{z_0} = 0$ or π. Here, mirror symmetry has been used to fold $\pm k_x$ and $\pm k_y$ so that (k_x, k_y) is restricted to the first quadrant of the first Brillouin zone (BZ). In this projected representation, the vHS effects are most pronounced at the center and the BZ boundaries.

Shown in Fig. 2 are the energy positions of the four types of vHSs in the momentum-integrated rf current $I(\nu)$, and their counterparts in the k_z-integrated momentum-resolved response $I(k, \nu)$ along the face-diagonal direction $\mathbf{k}_\parallel = (k, k)$. In the momentum-integrated spectra in Fig. 2(a), the M_1 vHS is the most prominent and should be experimentally accessible. Compared to the fully integrated signal, the vHS effects in the partially momentum-resolved spectrum in Fig. 2(b) are significantly more pronounced, because reducing the integration dimensionality better preserves the nonanalytic nature of the dispersion. Correspondingly, extracting the energy distribution curves (EDCs) from such partially momentum-resolved rf data is expected to yield unambiguous experimental signatures of these vHS features.

D. Phenomenological spectral broadening

In our initial theoretical framework, the spectral function exhibits infinitely sharp quasiparticle peaks. To simulate the finite lifetime of thermally excited pairs and single-particle scattering, we generalize the (retarded) self-energy to a phenomenological form, which was originally obtained from numerical studies [51,52] and applied in pseudogap research of high T_c superconductivity [46,53,54] and in rf spectroscopic studies of ultracold Fermi gases [47],

$$\Sigma_{pg}^R(\mathbf{k}, \omega) = \frac{\Delta_{pg}^2}{\omega + \xi_{\mathbf{k}} + i\Gamma_0} - i\Gamma_1, \quad (8)$$

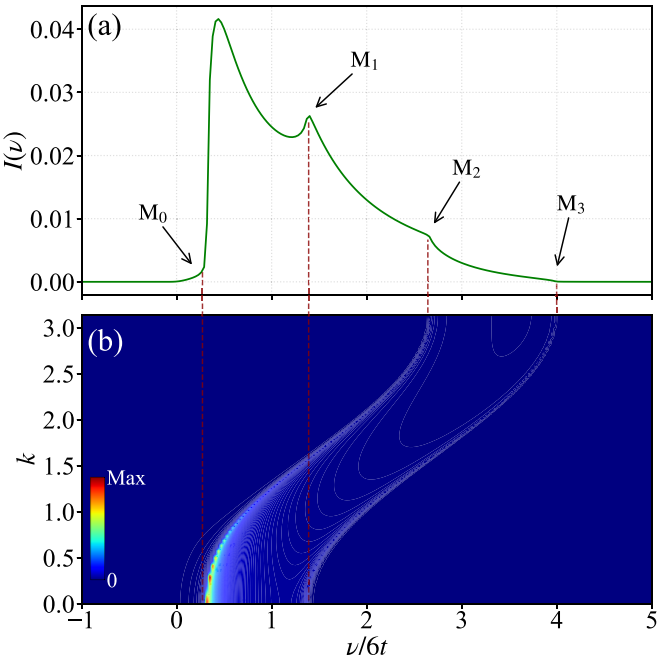


FIG. 2. (a) rf current $I(\nu)$, i.e., the momentum-integrated rf spectrum, at T_c for $U/6t = -1.8$ and $n = 0.1$. The four types of vHSs are labeled on the curve. (b) The z-integrated, partially momentum-resolved rf spectrum $I(k, \nu)$ plotted along the projected face-diagonal direction $\mathbf{k}_\parallel = (k, k)$. The red dashed lines align the corresponding vHS features in panels (a) and (b).

where Γ_0 describes the broadening of quasiparticle peaks associated with the finite pair lifetime, and Γ_1 accounts for the incoherent background from single-particle scattering. The full spectral function follows from Dyson's equation

$$A(\mathbf{k}, \omega) = \frac{-2\,\mathrm{Im}\Sigma_{pg}^R}{\left[\omega - \xi_{\mathbf{k}} - \Sigma_{sc}^R - \mathrm{Re}\Sigma_{pg}^R\right]^2 + \left[\mathrm{Im}\Sigma_{pg}^R\right]^2}. \quad (9)$$

In the results below, we treat Γ_0 and Γ_1 as adjustable phenomenological parameters to systematically assess the visibility and resolvability of the vHS features under realistic experimental conditions; both parameters become negligible at low temperatures due to the formation of stable pairing [55]. The broadened BCS form of the spectral function underlying Eq. (9) is well supported experimentally, as recent rf measurements in homogeneous unitary Fermi gases [43], together with earlier rf studies [41], have confirmed that the spectral function indeed retains a BCS-like two-branch structure even in the strongly interacting regime. We note that the vHS detunings in Eq. (5) follow from the resonance condition $\xi_{\mathbf{k}} - \nu + E_{\mathbf{k}} = 0$ and therefore define the underlying kinematic locations of the vHS features. The phenomenological broadening mainly smears these singular structures and serves to reduce their signal contrast. This broadening therefore weakens as the temperature decreases, consistent with recent momentum-resolved rf measurements on the homogeneous unitary Fermi gas [43], where the broadening increases with temperature. Far above T_c, the gap becomes small, and the large detunings are expected to weaken the vHS signals and can even cause neighboring vHS peaks to coalesce. Moreover,

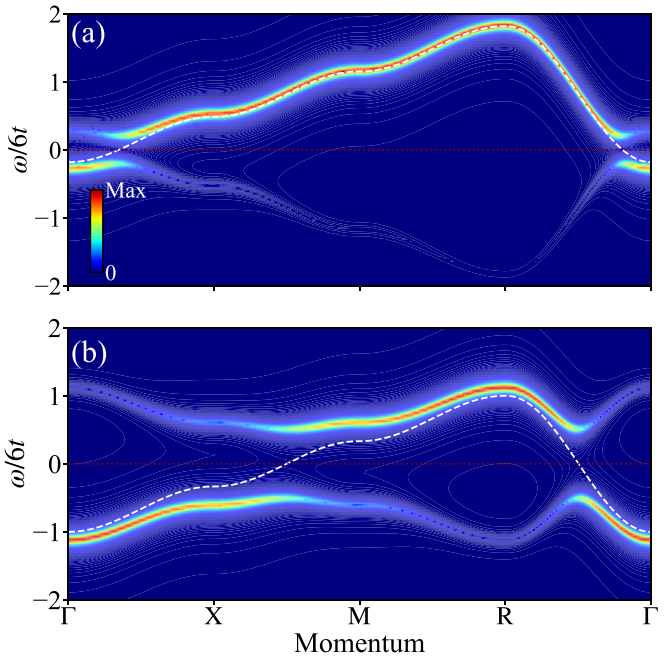


FIG. 3. Spectral function $A(\mathbf{k}, \omega)$ of the 3D attractive FHM at T_c and U_c for (a) $n = 0.1$ and (b) $n = 1$, with $\Gamma_0 = \Gamma_1 = 0.05$. The white dashed line denotes the noninteracting band dispersion.

at such high T, the frequency and momentum dependencies of the self-energy can no longer be neglected, which shifts the positions of the already broadened vHS peaks slightly and hence leads to quantitative deviations in the extracted Δ and μ.

III. NUMERICAL RESULTS AND DISCUSSION

A. Spectral function

Based on the self-consistent solutions, we evaluate the spectral function using Eq. (9) with $\Gamma_0 = \Gamma_1 = 0.05$. Figure 3 illustrates the qualitative evolution of $A(\mathbf{k}, \omega)$ for different densities (a) $n = 0.1$ and (b) $n = 1$ along the high-symmetry momentum directions at U_c and T_c. Results of more densities can be found in Appendix B. A pronounced gap opens at the Fermi surface for both densities. Along the Γ–R direction (the body diagonal), a characteristic backbending feature occurs at the Fermi wave vector $\mathbf{k}_\mu$ determined by $\xi_{\mathbf{k}_\mu} = 0$. At low filling, the spectral function along Γ–R resembles that of the 3D continuum limit, where $k_\mu \simeq \sqrt{\mu}$. As n increases, the gap widens and the spectral weight of the lower hole branch is enhanced, with lattice effects becoming increasingly apparent.

At half filling ($n = 1$), particle-hole symmetry fixes the chemical potential at the band center ($\mu = 1$). The corresponding Fermi-surface crossing along Γ–R is located at $\mathbf{k}_\mu = (\pi/2, \pi/2, \pi/2)$, i.e., exactly at the midpoint of the Γ–R line, as shown in Fig. 3(b). This special kinematic point provides a useful experimental diagnostic to identify half filling; combined with the vHS protocol proposed below, it enables Δ to be extracted from a single vHS measurement.

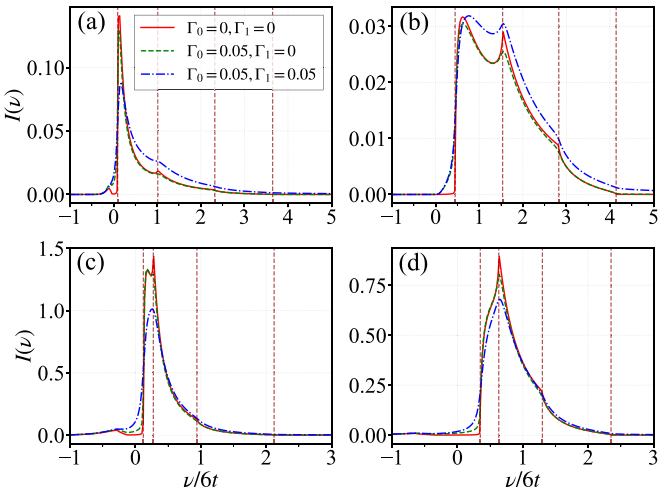


FIG. 4. rf current $I(\nu)$ as a function of detuning ν for (a) $n = 0.1$, $U = U_c$, (b) $n = 0.1$, $U/6t = -2$, (c) $n = 1$, $U = U_c$, and (d) $n = 1$, $U/6t = -2$, for various Γ_0 and Γ_1. The vertical lines indicate the rf detunings corresponding to the M_0–M_3 vHSs.

B. rf current and sensitivity to broadening

The fully momentum-integrated rf current $I(\nu)$ is the simplest experimental observable. We compute $I(\nu)$ for various (U, n) and examine the sensitivity of the vHS features to the broadening parameters Γ_0 and Γ_1.

As shown in Fig. 4, for a fixed filling, as the coupling increases from weak to strong, the pairing gap grows and the rf spectral weight shifts and spreads toward larger detuning, leading to a broader spectrum consistent with the observations in continuum gases [37]. The shift simultaneously suppresses the peak near the M_0 detuning at the left edge, making the M_1 vHS feature relatively more pronounced, as shown in Fig. 4(b). As the density (and chemical potential) increases toward half filling, the left-edge peak and the M_1 peak approach each other, and the spectral weight of the former becomes so suppressed that the M_1 peak becomes dominant. Upon broadening, the two features merge into a single dominant peak, as seen in Figs. 4(c) and 4(d). Compared with the low-filling case, the spectral peak at high filling is then associated primarily with the M_1 vHS, reflecting the proximity of the Fermi level to the vHS band extrema.

The broadenings primarily reduce the contrast of the vHS features and smear nearby structures, while their spectral weight remains concentrated near the kinematic detunings predicted by Eq. (5). The apparent peak or spectral maxima may change slightly when features overlap, but the underlying vHS markers are only weakly sensitive to Γ_0 and Γ_1 within the parameter range at low temperature. This supports the use of Eq. (5) as a stable guide for extracting Δ and μ from well-resolved spectral features. Note that the M_0 detuning, corresponding to the Γ point, provides a particularly strong marker in the large-gap regime, where it moves well away from zero detuning.

C. k_z-integrated momentum-resolved rf spectroscopy

The observable more directly accessible in experiments is the k_z-integrated, (k_x, k_y)-resolved spectrum $I(\mathbf{k}_\parallel, \nu)$, which

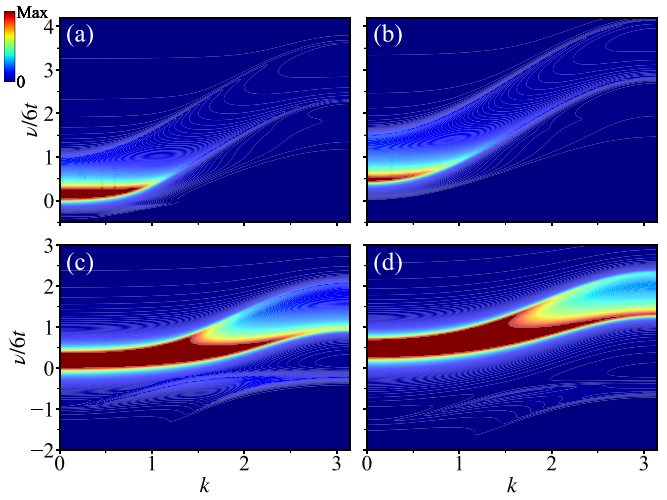


FIG. 5. The k_z-integrated, (k_x, k_y)-resolved rf spectra $I(k, \nu)$ at T_c along the face-diagonal direction $\mathbf{k}_\parallel = (k, k)$ for (a) $n = 0.1$, $U = U_c$, (b) $n = 0.1$, $U/6t = -2$, (c) $n = 1$, $U = U_c$, and (d) $n = 1$, $U/6t = -2$. The same color saturation value is applied across all panels to enhance the visibility of weak signals.

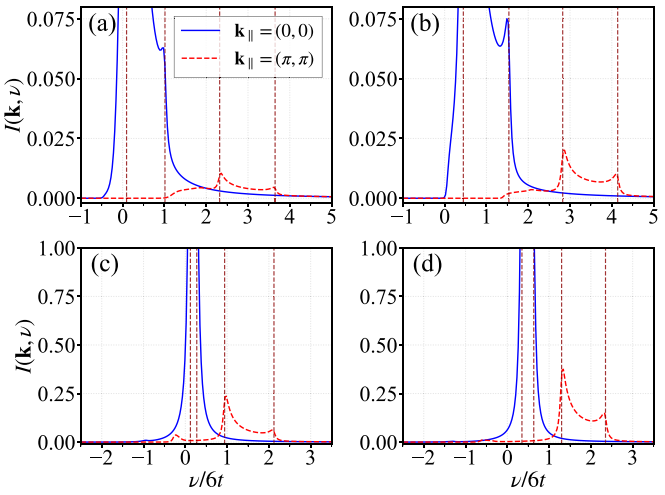


FIG. 6. EDCs $I(\mathbf{k}_\parallel, \nu)$ at the center and edge of the first Brillouin zone for (a) $n = 0.1$, $U = U_c$, (b) $n = 0.1$, $U = -2$, (c) $n = 1$, $U = U_c$, and (d) $n = 1$, $U = -2$. The blue solid and red dashed lines denote the EDCs at $\mathbf{k}_\parallel = (0, 0)$ and $\mathbf{k}_\parallel = (\pi, \pi)$, respectively. The vertical lines indicate the rf detunings corresponding to the M_0–M_3 vHSs.

retains the momentum resolution in the xy plane. We focus on the face-diagonal direction $\mathbf{k}_\parallel = (k, k)$ and axis-along direction $\mathbf{k}_\parallel = (0, k)$ with $\Gamma_0 = \Gamma_1 = 0.05$. In contrast to the fully integrated spectrum, where the M_1 feature dominates, the partial momentum resolution brings the M_2 and M_3 features to the foreground along the face-diagonal direction. As discussed below, however, the $\mathbf{k}_\parallel = (0, \pi)$ point turns out to be more favorable experimentally, since the M_1 and M_2 signals there are considerably stronger.

Comparing Figs. 5(a) and 5(b), increasing $|U|$ shifts the dominant spectral weight toward larger rf detunings, consistent with a larger pairing gap. When the filling increases to $n = 1$ [Figs. 5(c) and 5(d)], the spectral weight also shifts toward larger detunings as the pairing gap grows at these interaction strengths, while the spacing between the vHS features decreases. As shown in Fig. 3, this behavior reflects the reduced curvature of the dispersion near the relevant band extrema; as the Fermi level approaches the band edge, the dispersion flattens, which narrows the energy window available for the rf transitions.

To extract the vHS signatures, we plot the energy distribution curves $I(\mathbf{k}_\parallel, \nu)$ at the zone center $\mathbf{k}_\parallel = (0, 0)$ and zone corner $\mathbf{k}_\parallel = (\pi, \pi)$, as shown in Fig. 6. The EDCs at $\mathbf{k}_\parallel = (0, 0)$ exhibit stronger overall intensity due to larger occupied spectral weight. In contrast, the EDCs at $\mathbf{k}_\parallel = (\pi, \pi)$ show more pronounced vHS features, which become increasingly prominent as $|U|$ and n increase.

However, the EDC signal at (π, π) is weak, since M_2 and M_3 in Fig. 3 lie far above the Fermi level, so that the corresponding spectral weight, indicated by the opacity of the dispersion curves, is small and vanishes in the $U \to 0$ limit. To obtain stronger signals, we examine the EDCs at $\mathbf{k}_\parallel = (0, \pi)$, with k_z integrated, for the same parameters, as shown in Fig. 7. For both low and high fillings, the rf signals at $\mathbf{k}_\parallel = (0, \pi)$ are much stronger than those at (π, π), since the M_1 and M_2 features here lie closer to or below the Fermi level. The M_1 and M_2 features at $\mathbf{k}_\parallel = (0, \pi)$ are therefore considerably more robust than the M_2 and M_3 features at (π, π), for a given lattice size and total atom number in experiment.

D. vHS detunings as functions of interaction strength

Figure 8 shows the predicted vHS rf detunings ν_i as functions of $-U/6t$, computed from Eqs. (5) using the self-consistent (μ, Δ) for various n. This plot serves as the theoretical "map" connecting the measurable vHS positions to the underlying pairing parameters.

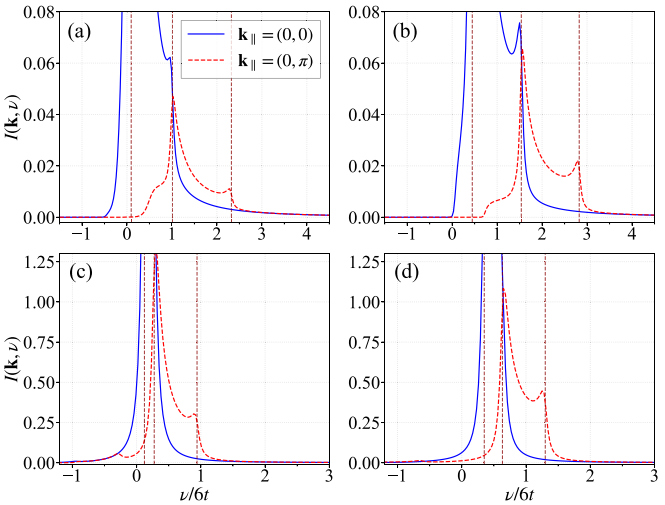


FIG. 7. EDCs $I(\mathbf{k}_\parallel, \nu)$ with the same (n, U) as in Fig. 6 but at $\mathbf{k}_\parallel = (0, 0)$ and $\mathbf{k}_\parallel = (0, \pi)$ in the xy plane of the first BZ. The blue solid and red dashed lines denote the cases of $\mathbf{k}_\parallel = (0, 0)$ and $\mathbf{k}_\parallel = (0, \pi)$, respectively. The vertical lines indicate the rf detunings corresponding to the M_0–M_2 vHSs.

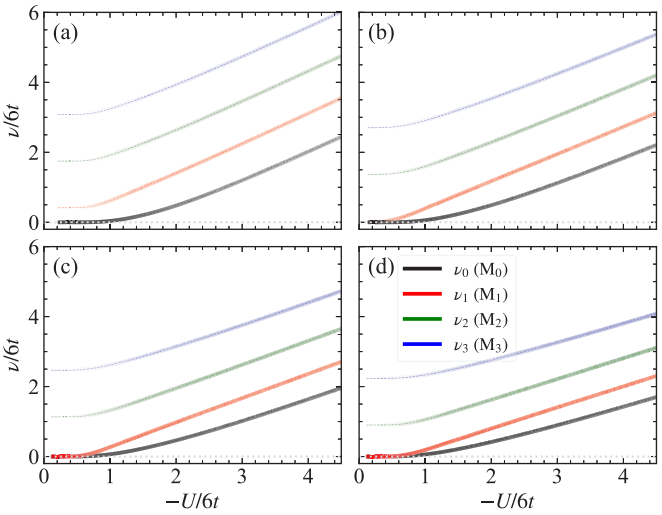


FIG. 8. vHS rf detunings ν_i ($i = 0, \ldots, 3$) as functions of $-U/6t$ for $n =$ (a) 0.2, (b) 0.4, (c) 0.6, and (d) 0.8, computed from the kinematic relation of Eq. (5) with the self-consistent (μ, Δ). The opacity of the curves is coded by the spectral weight $v_{\mathbf{k}}^2$ at the vHS momenta.

The detuning ν_0 starts from zero at $U = 0$, passes through an exponentially suppressed flat region, scaling approximately as Δ^2, and then rises away from the horizontal axis at stronger coupling. Meanwhile, ν_1, ν_2, and ν_3 are well separated from one another and grow monotonically with $|U|$, reflecting the increasing pairing gap, along with decreasing μ. Comparing the four panels, the vHS marker positions all decrease with increasing n, dominated by the chemical-potential term $\epsilon_i - \mu$ in Eq. (5) that shifts the band energies downward. The spectral weight, in contrast, is controlled by the coherence factor $v_{\mathbf{k}}^2$ and spreads toward larger momenta as the gap grows. The separation between ν_1, ν_2, and ν_3 across a wide coupling range indicates that multiple candidate vHS markers exist at the kinematic level.

It should be noted, however, that the spectral weight $v_{\mathbf{k}}^2$ contributing to the ν_1, ν_2, and ν_3 features becomes very small and vanishes at $U = 0$ for low fillings, consistent with the fact that the rf spectrum in the noninteracting limit reduces to a single δ-function peak at $\nu = 0$.

E. Extraction protocol for Δ and μ

The kinematic relations in Eq. (5) can be inverted algebraically. To illustrate the procedure, we outline the inversion for the M_1 and M_2 pair, which are well separated and experimentally favorable. Using the band energies $\epsilon_i = 2i/3$ ($i = 1, 2$) defined in Eq. (6), Eq. (5) can be rearranged to yield

$$\Delta^2 = \nu_i(\nu_i - 2\epsilon_i + 2\mu), \quad i = 1, 2. \tag{10}$$

Eliminating Δ^2 between the two equations gives μ directly, after which Δ follows from either equation. For concreteness, using the parameters of Fig. 4(c) ($n = 1, U = U_c$), the M_1 and M_2 detunings extracted from the spectrum yield $\mu \approx 1.0$ and $\Delta \approx 0.5$, in quantitative agreement with the self-consistent input values. Equivalent inversions can be performed for any pair of vHS features that are sufficiently resolved.

At half filling, $\mu = 1$, so that a single vHS measurement suffices:

$$\Delta = \sqrt{\nu_i(\nu_i - 2\epsilon_i + 2)}. \tag{11}$$

Thus, one may choose the most pronounced, best separated signals among the M_1, M_2, and M_3 features for the best quantitative accuracy.

It should be noted that the pairing gap Δ represents the off-diagonal part of the self-energy, while the chemical potential μ appearing in the kinematic relations is the effective one determined by the self-consistent equations. It differs from the physical value measured relative to the noninteracting band bottom by the bare Hartree shift $nU/2$ and the other diagonal self-energy contributions. These diagonal contributions do not vanish with the gap; indeed, in the limit $\Delta \to 0$, the full Green's function G reduces to the formally bare G_0, yet its μ may still differ from the noninteracting value.

IV. CONCLUSION

We have shown that van Hove singularities in the rf spectra of the 3D attractive Fermi-Hubbard model provide robust, kinematics-based markers for the pairing gap Δ and chemical potential μ. Four types of vHSs were classified, and their rf detuning positions were derived as simple algebraic functions of Δ and μ alone. This makes it possible, in principle, to extract both parameters from two well-resolved and sufficiently intense singular features without full spectral dispersion fitting. The features remain identifiable under realistic lifetime and scattering broadenings, become more visible at stronger coupling where backbending loses sensitivity, and reduce to a single-vHS diagnostic at half filling owing to particle-hole symmetry. In the k_z-integrated spectra, the EDCs at $\mathbf{k}_\parallel = (0, \pi)$ provide the strongest signals and are therefore the most favorable for experiments. We note that the present results are obtained within the pseudogap approximation $\Sigma_{\mathrm{pg}}(K) \approx -\Delta_{\mathrm{pg}}^2 G_0(-K)$, which captures the dominant $Q \approx 0$ contribution; a fully self-consistent convolution over all pair momenta would introduce additional frequency-dependent broadening, likely further softening the vHS features, and remains a challenge for future work. We also note that the present analysis employs the G_0G T-matrix scheme; in conserving, Φ-derivable (GG) or non-self-consistent (G_0G_0) formulations, the quantitative relation between vHS detunings and the pairing gap may differ, and the extent to which vHS features survive at these levels of approximation warrants further investigation. More broadly, the kinematic relations derived here are independent of the concrete details of a particular many-body framework, provided that the propagator of the theory retains a BCS-like pole structure with a real, roughly momentum-independent Δ and an effective μ. Indeed, such a BCS-like form has been validated by various BCS-BEC crossover studies in the continuum, employing the conserving GG theory [26], the G_0G scheme [47], the non-self-consistent G_0G_0 approximation [56], and finite-temperature quantum Monte Carlo [57], all of which analyze their spectra in terms of the same BCS-like dispersion, albeit with quantitatively different pairing gap values. Most importantly, it is confirmed by a recent microwave spectroscopic experiment [43]. Therefore, vHS-based gap extraction can serve as a useful

cross-method benchmark and test bed, so that the parameters inferred from experiment may be used to test against the values predicted by these different T-matrix theories, cluster dynamical mean-field theory, and other approaches that currently yield disparate gap estimates. Recent experimental advances in 3D lattice cooling and homogeneous trapping [58], together with rf frequency resolutions reaching $0.038\,E_F$ [43,59], make these predictions testable with current technology. We anticipate that vHS-based extraction will serve as a practical complement to backbending and peak-analysis methods in ongoing quantum simulation experiments.

ACKNOWLEDGMENT

This work was supported by Quantum Science and Technology—National Science and Technology Major Project (Grant No. 2021ZD0301904).

DATA AVAILABILITY

There are no publicly available research data or software supporting this manuscript. Requests for further information or data should be sent to the authors.

APPENDIX A: PAIR-FLUCTUATION THEORY: DETAILED FORMALISM

Here, we provide the full self-consistent pair-fluctuation formalism used in the main text, closely following Refs. [39,45].

1. Hamiltonian and T-matrix

The attractive Fermi-Hubbard model in momentum space is

$$H-\mu\hat{N}=\sum_{\mathbf{k}\sigma}\xi_{\mathbf{k}}c^{\dagger}_{\mathbf{k}\sigma}c_{\mathbf{k}\sigma}+U\sum_{\mathbf{k}\mathbf{k}'\mathbf{q}}c^{\dagger}_{\mathbf{k}+\frac{\mathbf{q}}{2}\uparrow}c^{\dagger}_{-\mathbf{k}+\frac{\mathbf{q}}{2}\downarrow}c_{-\mathbf{k}'+\frac{\mathbf{q}}{2}\downarrow}c_{\mathbf{k}'+\frac{\mathbf{q}}{2}\uparrow}, \tag{A1}$$

with $\xi_{\mathbf{k}}=\epsilon_{\mathbf{k}}-\mu$, $\epsilon_{\mathbf{k}}=2t(3-\cos k_x-\cos k_y-\cos k_z)$, and $U<0$. The critical coupling $U_c=-1/\sum_{\mathbf{k}}1/(2\epsilon_{\mathbf{k}})\approx -7.9136t$ marks the unitary point.

The fermion self-energy contains condensate and pseudogap contributions:

$$\Sigma(K)=\Sigma_{sc}(K)+\Sigma_{pg}(K), \tag{A2a}$$

$$\Sigma_{sc}(K)=-\Delta^2_{sc}G_0(-K)=\frac{\Delta^2_{sc}}{i\omega_l+\xi_{\mathbf{k}}}, \tag{A2b}$$

$$\Sigma_{pg}(K)=\sum_{Q}t_{pg}(Q)G_0(Q-K), \tag{A2c}$$

where $K=(i\omega_l,\mathbf{k})$, $Q=(i\Omega_n,\mathbf{q})$ are four-momenta, with $\sum_K\equiv T\sum_l\sum_{\mathbf{k}}$, and $G_0(K)=(i\omega_l-\xi_{\mathbf{k}})^{-1}$ is the bare Green's function.

The finite-momentum T-matrix sums the ladder diagrams:

$$t_{pg}(Q)=\frac{U}{1+U\chi(Q)}, \tag{A3}$$

with the pair susceptibility $\chi(Q)=\sum_K G(K)G_0(Q-K)$ including self-energy feedback through the full Green's function $G(K)$—a key distinction from the Nozières–Schmitt-Rink approach [21].

The Thouless criterion $t^{-1}_{pg}(0)=0$ implies that the dominant contribution to Σ_{pg} comes from $Q\approx 0$, leading to the pseudogap approximation $\Sigma_{pg}(K)\approx-\Delta^2_{pg}G_0(-K)$, with

$$\Delta^2_{pg}=-\sum_{Q\neq 0}t_{pg}(Q). \tag{A4}$$

The total pairing gap is $\Delta=\sqrt{\Delta^2_{sc}+\Delta^2_{pg}}$.

2. Self-consistent equations

The full Green's function takes the BCS form

$$G(K)=\frac{u^2_{\mathbf{k}}}{i\omega_l-E_{\mathbf{k}}}+\frac{v^2_{\mathbf{k}}}{i\omega_l+E_{\mathbf{k}}}, \tag{A5}$$

with $u^2_{\mathbf{k}}, v^2_{\mathbf{k}}=(1\pm\xi_{\mathbf{k}}/E_{\mathbf{k}})/2$ and $E_{\mathbf{k}}=\sqrt{\xi^2_{\mathbf{k}}+\Delta^2}$.

The gap equation is

$$1+U\sum_{\mathbf{k}}\frac{1-2f(E_{\mathbf{k}})}{2E_{\mathbf{k}}}=a_0\mu_{pair}, \tag{A6}$$

where $f(x)$ is the Fermi distribution, the effective pair chemical potential $\mu_{pair}=0$ for $T\leqslant T_c$, and a_0 is an expansion coefficient of the inverse T-matrix.

The particle number equation is

$$n=2\sum_{\mathbf{k}}\left[v^2_{\mathbf{k}}+\frac{\xi_{\mathbf{k}}}{E_{\mathbf{k}}}f(E_{\mathbf{k}})\right]. \tag{A7}$$

The pseudogap equation follows from a Taylor expansion of $t^{-1}_{pg}(Q)$ on the real frequency axis, $t^{-1}_{pg}(\Omega,\mathbf{q})\approx a_1\Omega^2+a_0(\Omega-\Omega^0_{\mathbf{q}}+\mu_{pair})$, yielding

$$|a_0|\Delta^2_{pg}=\sum_{\mathbf{q}}\left[1+4\frac{a_1}{a_0}\left(\Omega^0_{\mathbf{q}}-\mu_{pair}\right)\right]^{-1/2}b(\Omega_{\mathbf{q}}), \tag{A8}$$

where $\Omega_{\mathbf{q}}=\{\sqrt{a_0^2[1+4a_1(\Omega^0_{\mathbf{q}}-\mu_{pair})/a_0]}-a_0\}/2a_1$ is the pair dispersion, with $\Omega^0_{\mathbf{q}}=2B(3-\cos q_x-\cos q_y-\cos q_z)$, B is the pair hopping integral, and $b(x)$ is the Bose distribution function.

Equations (A6)–(A8) form a closed set, solved self-consistently for (μ,Δ_{pg},T_c) at $\Delta_{sc}=0$, and for (μ,Δ,Δ_{pg}) below T_c. When extended to above T_c, they can be solved for $(\mu,\Delta_{pg},\mu_{pair})$ as a function of $T>T_c$.

APPENDIX B: ADDITIONAL NUMERICAL RESULTS FOR DIFFERENT DENSITIES

In this Appendix, we provide additional numerical data for filling factors $n=0.2$, 0.4, 0.6, and 0.8, complementing the representative cases $n=0.1$ and $n=1$ presented in the main text, which represent low and high fillings, respectively. The broadening parameters are set to $\Gamma_0=\Gamma_1=0.05$ throughout.

1. rf current at different densities

As shown in Figs. 9 and 10, the weight of the pairing peaks gradually decreases and the M_1 vHS peak becomes progressively dominant as n increases, reflecting the growing

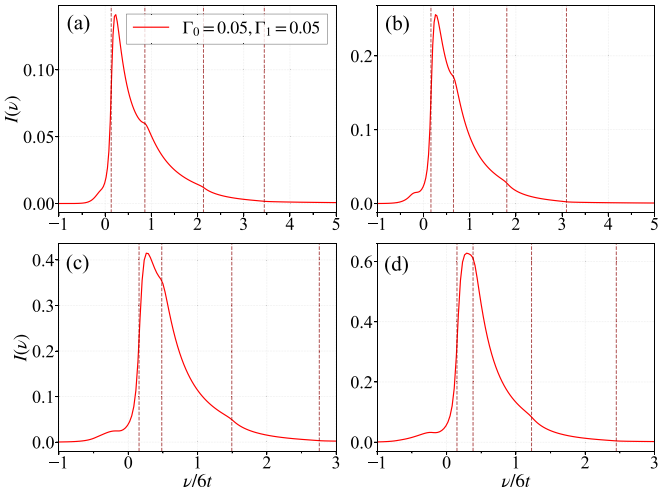


FIG. 9. Rf current for densities $n = 0.2$, 0.4, 0.6, and 0.8 at $U = U_c$. The vertical lines indicate the rf detunings corresponding to the M_0–M_3 vHSs.

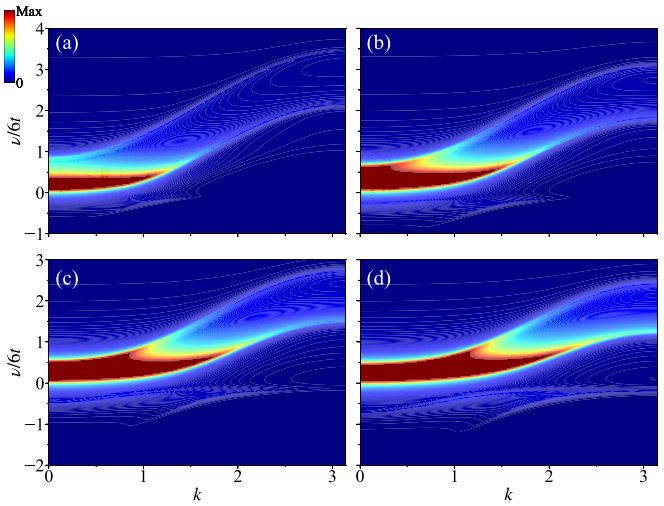


FIG. 11. k_z-integrated momentum-resolved rf spectra $I(\mathbf{k}_\parallel, \nu)$ along the face-diagonal direction $\mathbf{k}_\parallel = (k, k)$ for densities $n = 0.2$, 0.4, 0.6, and 0.8 at $U = U_c$.

prominence of lattice effects. The rf detuning ν_1 corresponding to the M_1 vHS decreases, as the chemical potential approaches the M_1 band energy $\epsilon_1 = 2/3$ from below (see Fig. 15). For fixed density, increasing $|U|$ shifts the M_1 vHS to larger detuning, signaling an enlarged pairing gap.

2. k_z-integrated momentum-resolved rf spectra

As n increases, the spectral weight distribution narrows because the hole branch of the quasiparticle dispersion shifts, moving spectral weight to smaller detuning, which reflects the concurrent changes in the pairing gap and the chemical potential. Inspection of the unified expression for ν_i in the main text reveals that this change is dominated by the decrease of $|\epsilon_i - \mu|$, as the Fermi surface moves closer to the relevant vHS band energy with increasing n. This density-dependent spectral evolution is evident in Figs. 11 and 12 for $U = U_c$ and $U/6t = -2$, respectively.

3. Energy distribution curves

As shown in Figs. 13 and 14 for $U = U_c$ and $U/6t = -2$, respectively, the EDCs exhibit more pronounced VHS evolution than the momentum-integrated spectra because fixing the two remaining momentum components leaves the VHS structure unaveraged along those directions. At $\mathbf{k}_\parallel = (0, 0)$,

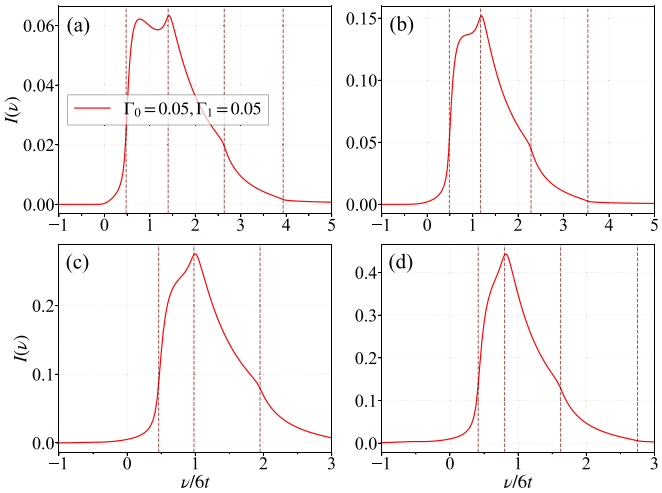


FIG. 10. rf current for densities $n = 0.2$, 0.4, 0.6, and 0.8 at $U/6t = -2$. The vHS signatures become more pronounced at stronger coupling. The vertical lines indicate the rf detunings corresponding to the M_0–M_3 vHSs.

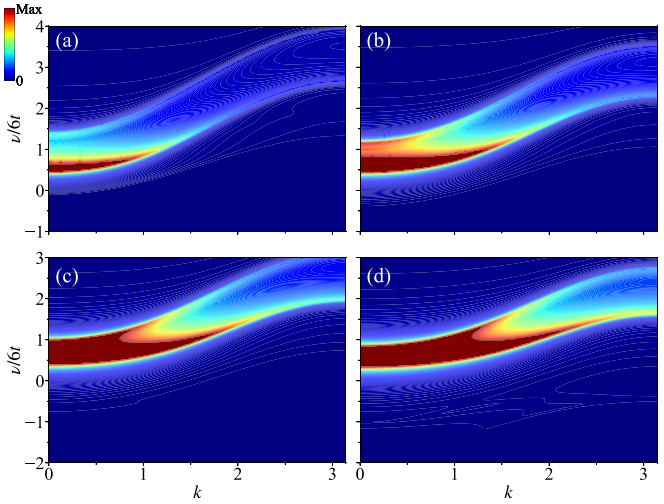


FIG. 12. k_z-integrated momentum-resolved rf spectra $I(\mathbf{k}_\parallel, \nu)$ along the face-diagonal direction $\mathbf{k}_\parallel = (k, k)$ for densities $n = 0.2$, 0.4, 0.6, and 0.8 at $U/6t = -2$.

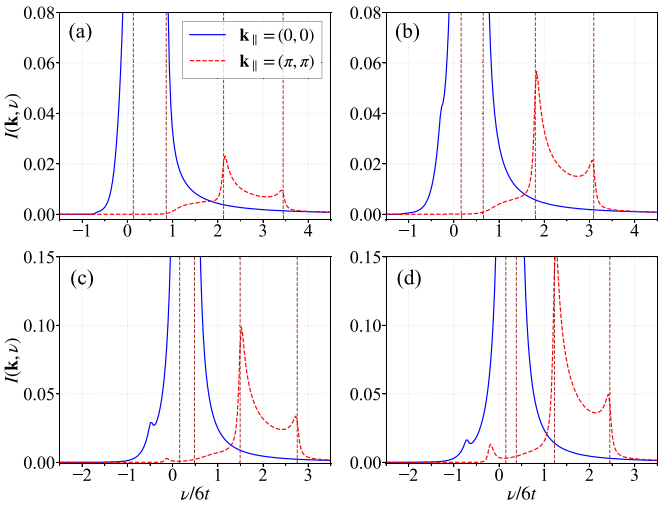


FIG. 13. EDCs extracted from the k_z-integrated momentum-resolved rf spectra for densities $n = 0.2$, 0.4, 0.6, and 0.8 at $U = U_c$. The vertical lines indicate the rf detunings corresponding to the M_0–M_3 vHSs.

the M_0 and M_1 vHSs have greater signal intensity, but their detunings lie close to zero when the gap is not large enough, making them susceptible to background contamination, especially from the trap edge in a realistic experimental setup. The M_2 and M_3 vHSs at $\mathbf{k}_\parallel = (\pi, \pi)$, in contrast, are more clearly separated in the plots. In the main text, we further find that the M_1 and M_2 vHSs in the spectrum at $\mathbf{k}_\parallel = (0, \pi)$ have stronger intensities and are therefore the most robust choice for experiments. Here, we show the curves for $\mathbf{k}_\parallel = (\pi, \pi)$ for illustrative purposes, where the vHS features are more clearly separated from their counterparts at $\mathbf{k}_\parallel = (0, 0)$.

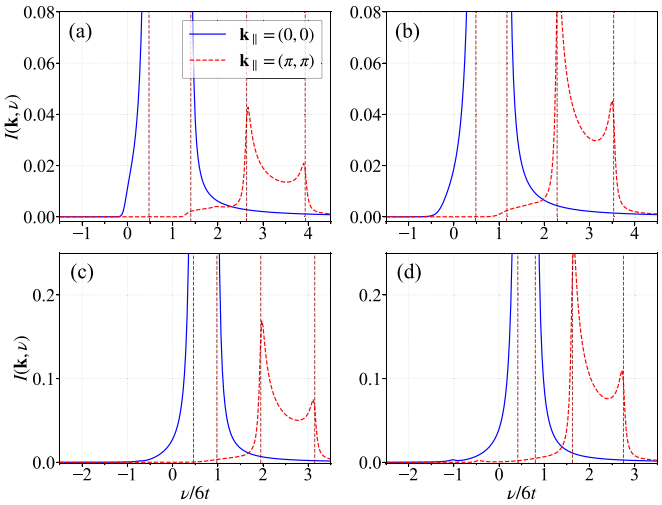


FIG. 14. EDCs for densities $n = 0.2$, 0.4, 0.6, and 0.8 at $U/6t = -2$. The vertical lines indicate the rf detunings corresponding to the M_0–M_3 vHSs.

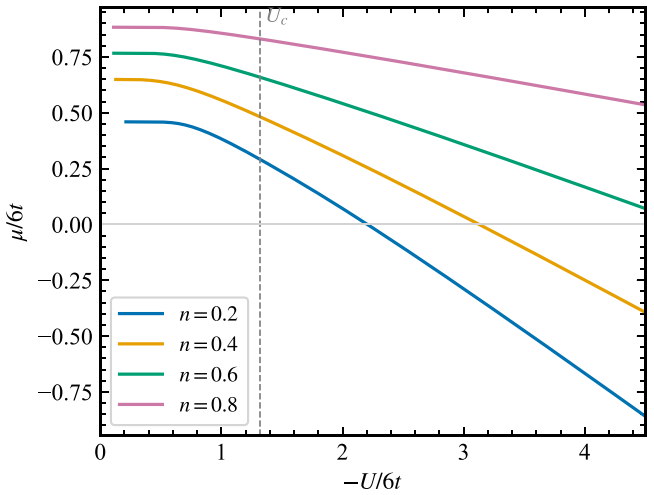


FIG. 15. Chemical potential $\mu/6t$ as a function of $-U/6t$ for fillings $n = 0.2$, 0.4, 0.6, and 0.8. The vertical dashed line marks the unitary coupling $U = U_c$.

4. Self-consistent parameters

To make the parametric dependence explicit, we report the self-consistent solutions of the pair-fluctuation theory as functions of $-U/6t$ for fillings $n = 0.2$, 0.4, 0.6, and 0.8, as shown in Figs. 15 and 16.

As $|U|$ increases, the pairing gap grows monotonically while the chemical potential decreases, crossing zero as the system enters the BEC regime. For fixed $-U/6t$, a larger filling n yields both larger μ and larger Δ, consistent with BCS-BEC crossover physics on the lattice.

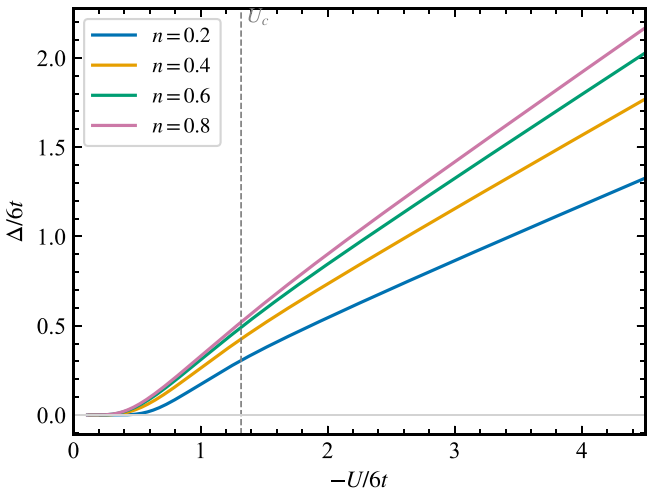


FIG. 16. Pairing gap $\Delta/6t$ as a function of $-U/6t$ for fillings $n = 0.2$, 0.4, 0.6, and 0.8. The vertical dashed line marks $U = U_c$.

[1] Q. J. Chen, J. Stajic, S. N. Tan, and K. Levin, BCS–BEC crossover: From high temperature superconductors to ultracold superfluids, Phys. Rep. **412**, 1 (2005).

[2] I. Bloch, J. Dalibard, and W. Zwerger, Many-body physics with ultracold gases, Rev. Mod. Phys. **80**, 885 (2008).

[3] Edited by W. Zwerger, *The BCS-BEC Crossover and the Unitary Fermi Gas* (Springer Science & Business Media, Berlin, Heidelberg, 2011), Vol. 836.

[4] I. Bloch, J. Dalibard, and S. Nascimbène, Quantum simulations with ultracold quantum gases, Nat. Phys. **8**, 267 (2012).

[5] R. A. Hart, P. M. Duarte, T.-L. Yang, X. Liu, T. Paiva, E. Khatami, R. T. Scalettar, N. Trivedi, D. A. Huse, and R. G. Hulet, Observation of antiferromagnetic correlations in the Hubbard model with ultracold atoms, Nature (London) **519**, 211 (2015).

[6] C. Gross and I. Bloch, Quantum simulations with ultracold atoms in optical lattices, Science **357**, 995 (2017).

[7] D. Jaksch, C. Bruder, J. I. Cirac, C. W. Gardiner, and P. Zoller, Cold bosonic atoms in optical lattices, Phys. Rev. Lett. **81**, 3108 (1998).

[8] C. Chin, R. Grimm, P. Julienne, and E. Tiesinga, Feshbach resonances in ultracold gases, Rev. Mod. Phys. **82**, 1225 (2010).

[9] T. Timusk and B. Statt, The pseudogap in high-temperature superconductors: An experimental survey, Rep. Prog. Phys. **62**, 61 (1999).

[10] Q. J. Chen, I. Kosztin, B. Jankó, and K. Levin, Pairing fluctuation theory of superconducting properties in underdoped to overdoped cuprates, Phys. Rev. Lett. **81**, 4708 (1998).

[11] Q. J. Chen, Z. Q. Wang, R. Boyack, S. L. Yang, and K. Levin, When superconductivity crosses over: From BCS to BEC, Rev. Mod. Phys. **96**, 025002 (2024).

[12] R. T. Scalettar, E. Y. Loh, J. E. Gubernatis, A. Moreo, S. R. White, D. J. Scalapino, R. L. Sugar, and E. Dagotto, Phase diagram of the two-dimensional negative-U Hubbard model, Phys. Rev. Lett. **62**, 1407 (1989).

[13] B. Kyung, S. Allen, and A.-M. S. Tremblay, Pairing fluctuations and pseudogaps in the attractive Hubbard model, Phys. Rev. B **64**, 075116 (2001).

[14] C. Honerkamp and W. Hofstetter, Ultracold fermions and the SU(N) Hubbard model, Phys. Rev. Lett. **92**, 170403 (2004).

[15] R. Mondaini, P. Nikolić, and M. Rigol, Mott-insulator–to–superconductor transition in a two-dimensional superlattice, Phys. Rev. A **92**, 013601 (2015).

[16] A. Moreo and D. J. Scalapino, Cold attractive spin polarized Fermi lattice gases and the doped positive U Hubbard model, Phys. Rev. Lett. **98**, 216402 (2007).

[17] T. Paiva, R. R. dos Santos, R. T. Scalettar, and P. J. H. Denteneer, Critical temperature for the two-dimensional attractive Hubbard model, Phys. Rev. B **69**, 184501 (2004).

[18] V. B. Shenoy, Phase diagram of the attractive Hubbard model with inhomogeneous interactions, Phys. Rev. B **78**, 134503 (2008).

[19] R. Micnas, J. Ranninger, and S. Robaszkiewicz, Superconductivity in narrow-band systems with local nonretarded attractive interactions, Rev. Mod. Phys. **62**, 113 (1990).

[20] L. Gor'kov and T. Melik-Barkhudarov, Contribution to the theory of superfluidity in an imperfect Fermi gas, Sov. Phys. JETP **13**, 1018 (1961).

[21] P. Noziöres and S. Schmitt-Rink, Bose condensation in an attractive fermion gas: From weak to strong coupling superconductivity, J. Low Temp. Phys. **59**, 195 (1985).

[22] L. P. Kadanoff and P. C. Martin, Theory of many-particle systems. II. Superconductivity, Phys. Rev. **124**, 670 (1961).

[23] Q. J. Chen, Generalization of BCS theory to short coherence length superconductors: A BCS-Bose-Einstein crossover scenario, Ph.D. thesis, University of Chicago, 2000; see also arXiv:1801.06266.

[24] O. Tchernyshyov, Noninteracting Cooper pairs inside a pseudogap, Phys. Rev. B **56**, 3372 (1997).

[25] R. Haussmann, Properties of a Fermi liquid at the superfluid transition in the crossover region between BCS superconductivity and Bose-Einstein condensation, Phys. Rev. B **49**, 12975 (1994).

[26] R. Haussmann, M. Punk, and W. Zwerger, Spectral functions and rf response of ultracold fermionic atoms, Phys. Rev. A **80**, 063612 (2009).

[27] U. Schneider, L. Hackermüller, J. P. Ronzheimer, S. Will, S. Braun, T. Best, I. Bloch, E. Demler, S. Mandt, D. Rasch, and A. Rosch, Fermionic transport and out-of-equilibrium dynamics in a homogeneous Hubbard model with ultracold atoms, Nat. Phys. **8**, 213 (2012).

[28] D. Mitra, P. T. Brown, E. Guardado-Sanchez, S. S. Kondov, T. Devakul, D. A. Huse, P. Schauß, and W. S. Bakr, Quantum gas microscopy of an attractive Fermi–Hubbard system, Nat. Phys. **14**, 173 (2018).

[29] L. Hackermüller, U. Schneider, M. Moreno-Cardoner, T. Kitagawa, T. Best, S. Will, E. Demler, E. Altman, I. Bloch, and B. Paredes, Anomalous expansion of attractively interacting fermionic atoms in an optical lattice, Science **327**, 1621 (2010).

[30] M. Gall, C. F. Chan, N. Wurz, and M. Köhl, Simulating a Mott insulator using attractive interaction, Phys. Rev. Lett. **124**, 010403 (2020).

[31] P. T. Brown, E. Guardado-Sanchez, B. M. Spar, E. W. Huang, T. P. Devereaux, and W. S. Bakr, Angle-resolved photoemission spectroscopy of a Fermi–Hubbard system, Nat. Phys. **16**, 26 (2020).

[32] D.-Z. Zhu *et al.*, Observation of superfluidity in a 3D attractive fermionic Hubbard model (unpublished).

[33] P. Törmä, Physics of ultracold Fermi gases revealed by spectroscopies, Phys. Scr. **91**, 043006 (2016).

[34] C. J. Vale and M. Zwierlein, Spectroscopic probes of quantum gases, Nat. Phys. **17**, 1305 (2021).

[35] P. Törmä and P. Zoller, Laser probing of atomic Cooper pairs, Phys. Rev. Lett. **85**, 487 (2000).

[36] C. Chin, M. Bartenstein, A. Altmeyer, S. Riedl, S. Jochim, J. Denschlag, and R. Grimm, Observation of the pairing gap in a strongly interacting Fermi gas, Science **305**, 1128 (2004).

[37] C. H. Schunck, Y.-I. Shin, A. Schirotzek, and W. Ketterle, Determination of the fermion pair size in a resonantly interacting superfluid, Nature (London) **454**, 739 (2008).

[38] A. Schirotzek, Y.-I. Shin, C. H. Schunck, and W. Ketterle, Determination of the superfluid gap in atomic Fermi gases by quasiparticle spectroscopy, Phys. Rev. Lett. **101**, 140403 (2008).

[39] Q. J. Chen, Y. He, C.-C. Chien, and K. Levin, Theory of radio frequency spectroscopy experiments in ultracold Fermi gases and their relation to photoemission in the cuprates, Rep. Prog. Phys. **72**, 122501 (2009).

[40] J. T. Stewart, J. P. Gaebler, and D. S. Jin, Using photoemission spectroscopy to probe a strongly interacting Fermi gas, Nature (London) **454**, 744 (2008).

[41] J. P. Gaebler, J. T. Stewart, T. E. Drake, D. S. Jin, A. Perali, P. Pieri, and G. C. Strinati, Observation of pseudogap behaviour in a strongly interacting Fermi gas, Nat. Phys. **6**, 569 (2010).

[42] Y. Sagi, T. E. Drake, R. Paudel, R. Chapurin, and D. S. Jin, Breakdown of the Fermi liquid description for strongly interacting fermions, Phys. Rev. Lett. **114**, 075301 (2015).

[43] X. Li, S. Wang, X. Luo, Y.-Y. Zhou, K. Xie, H.-C. Shen, Y.-Z. Nie, Q. J. Chen, H. Hu, Y.-A. Chen, X.-C. Yao, and J.-W. Pan, Observation and quantification of the pseudogap in unitary Fermi gases, Nature (London) **626**, 288 (2024).

[44] S. Datta, V. N. Singh, and P. Majumdar, Radio-frequency spectroscopy of the attractive Hubbard model in a trap, Phys. Rev. A **89**, 053609 (2014).

[45] Q. J. Chen, I. Kosztin, B. Jankó, and K. Levin, Superconducting transitions from the pseudogap state: d-wave symmetry, lattice, and low-dimensional effects, Phys. Rev. B **59**, 7083 (1999).

[46] Q. J. Chen, K. Levin, and I. Kosztin, Superconducting phase coherence in the presence of a pseudogap: Relation to specific heat, tunneling, and vortex core spectroscopies, Phys. Rev. B **63**, 184519 (2001).

[47] Q. J. Chen and K. Levin, Momentum resolved radio frequency spectroscopy in trapped Fermi gases, Phys. Rev. Lett. **102**, 190402 (2009).

[48] G. Czycholl, *Solid State Theory, Vol. 1: Basics: Phonons and Electrons in Crystals* (Springer Nature, Berlin, Heidelberg, 2023).

[49] P. Pieri, L. Pisani, and G. C. Strinati, BCS-BEC crossover at finite temperature in the broken-symmetry phase, Phys. Rev. B **70**, 094508 (2004).

[50] R. Haussmann, Crossover from BCS superconductivity to Bose-Einstein condensation: A self-consistent theory, Z. Phys. B **91**, 291 (1993).

[51] J. Maly, Pseudogap effects in a precursor superconductivity model of the cuprates, Ph.D. thesis, University of Chicago, 1997, see Eq. (4.9).

[52] J. Maly, B. Jankó, and K. Levin, Numerical studies of the s-wave pseudogap state and related T_c: The "pairing approximation" theory, Physica C **321**, 113 (1999).

[53] M. R. Norman, M. Randeria, H. Ding, and J. C. Campuzano, Phenomenology of the low-energy spectral function in high-T_c superconductors, Phys. Rev. B **57**, R11093 (1998).

[54] Q. J. Chen and K. Levin, Phenomenological theory of the protected nodes and collapse of the Fermi arcs in underdoped cuprate superconductors, Phys. Rev. B **78**, 020513(R) (2008).

[55] C. P. Li, L. Sun, K. C. Zhang, J. R. Wu, Y. X. Wu, D. L. Yuan, P. Y. Chen, and Q. J. Chen, Rf spectra and pseudogap in ultracold Fermi gases across the BCS-BEC crossover from pairing fluctuation theory, arXiv:2604.06004.

[56] M. D. Reichl and E. J. Mueller, Quasiparticle dispersions and lifetimes in the normal state of the BCS-BEC crossover, Phys. Rev. A **91**, 043627 (2015).

[57] P. Magierski, G. Wlazłowski, A. Bulgac, and J. E. Drut, Finite-temperature pairing gap of a unitary Fermi gas by quantum Monte Carlo calculations, Phys. Rev. Lett. **103**, 210403 (2009).

[58] H.-J. Shao, Y.-X. Wang, D.-Z. Zhu, Y.-S. Zhu, H.-N. Sun, S.-Y. Chen, C. Zhang, Z.-J. Fan, Y. Deng, X.-C. Yao, Y.-A. Chen, and J.-W. Pan, Antiferromagnetic phase transition in a 3D fermionic Hubbard model, Nature (London) **632**, 267 (2024).

[59] K. K. Nielsen, M. Zwierlein, and G. M. Bruun, Dual spectroscopy of quantum simulated Fermi-Hubbard systems, Phys. Rev. Lett. **135**, 043401 (2025).